Journal of Solid State Chemistry 182 (2009) 2785–2790

Contents lists available at ScienceDirect

Journal of Solid State Chemistry

journal homepage: www.elsevier.com/locate/jssc

Synthesis and visible light photocatalysis of Fe-doped TiO_2 mesoporous layers deposited on hollow glass microbeads

Lifeng Cui, Yuansheng Wang *, Mutong Niu, Guoxin Chen, Yao Cheng

State Key Laboratory of Structural Chemistry, Fujian Institute of Research on the Structure of Matter, Chinese Academy of Sciences; Graduate School of Chinese Academy of Sciences, Fuzhou, Fujian 350002, China

ARTICLE INFO

Article history:
Received 27 April 2009
Received in revised form
23 July 2009
Accepted 24 July 2009
Available online 3 August 2009

Keywords:
Nano TiO_2
Fe doping
Hollow glass microbeads
Mesoporous structure
Photocatalysis

ABSTRACT

Nano-composite of Fe-doped anatase TiO_2 nanocrystals loaded on the hollow glass microbeads was prepared by co-thermal hydrolysis deposition and calcining treatment. The adherence of TiO_2 mesoporous layers to the surfaces of hollow glass microbeads prevented the aggregation of TiO_2 nanoparticles and benefited to their catalytic activity. The doping of Fe ions makes the absorption edge of the TiO_2 based nano-composite red-shifted into the visible region. An effective photodegradation of the methyl orange aqueous solution was achieved under visible light ($\lambda > 420$ nm) irradiation, revealing the potential applicability of such nano-composite in some industry fields, such as air and water purifications.

1. Introduction

In the last decade, nano-structured TiO_2 has been developed and used as a photocatalyst for air and water purifications because of its excellent photocatalytic activity, physical and chemical stability, and nontoxicity [1–8]. But for its wide band gap (3.0 eV for the rutile and 3.2 eV for the anatase phase), it only makes use of the ultraviolet light which contains merely a small portion (about 3–5%) of the sunlight's energy [9]. In order to develop more efficient photocatalyst, various methods have been used to improve the optical properties of TiO_2 by modifying its band gap, such as doping with other elements, sensitizing with dyes, coating the surface with noble metals or other semiconductors [7,10–15]. Among them, doping is a practical approach because the properties of the material are largely determined by chemical nature of the atoms or ions and of the bonds between them. Through doping with certain metallic or nonmetallic elements, it has been demonstrated that the photocatalytic feature of TiO_2 became visible light responsible [15–18]. Because of the small size of the cations than the anions, the Ti^{4+} cations could be replaced by other transition metal ions more easily than O^{2-} anion by other anions. It is believed that the small size of the TiO_2 nanoparticle is beneficial to the modification of its chemical composition due to the higher tolerance of the structural distortion induced by the inherent lattice strain in nanomaterials than that in their bulk counterparts [19]. Transition metal ions implanted into the TiO_2 crystalline lattice may introduce an impurity level into the band gap of TiO_2 and thus benefits to the photocatalysis. Choi et al. found that TiO_2 doped with Fe^{3+} exhibited the highest photocatalytic activity among those doped with other transition metal elements on the oxidation of $CHCl_3$ and the reduction of CCl_4 [20].

But only optical characteristic modification is not sufficient for the practical photocatalytic application of TiO_2 powder. It is necessary to deposit the catalyst onto the supports, because when the TiO_2 powder is put in a pool of polluted water, it will settle at the bottom and coagulate in the process of photodegradation, inducing the reduction of its catalytic effectiveness [21]. In addition, TiO_2 as catalyst is usually nano-scaled powder with high surface activity, thus is difficult to separate from water completely and be reused. In order to solve these problems, various materials, such as glass, quartz, wool, steel, etc. have been used as the substrates for TiO_2 powder [22,23].

In present work, nano-composite with Fe-doped TiO_2 nanocrystals deposited on the aluminosilicate hollow glass microbeads (HGMBs) was fabricated by a simple and green co-thermal hydrolysis deposition in the acidic water solution. The UV–Vis diffuse reflectance spectroscopy indicated that the absorption edge of the TiO_2 based nano-composite red-shifted into the visible

* Corresponding author. Fax: +86 591 83705402.
E-mail address: yswang@fjirsm.ac.cn (Y. Wang).

0022-4596/$ - see front matter © 2009 Elsevier Inc. All rights reserved.
doi:10.1016/j.jssc.2009.07.045

region, and the photocatalytic efficiency reached 39% for 7 h photodegradation of the 10^{-5} M methyle orange aqueous solution under visible light ($\lambda > 420$ nm) irradiation.

2. Experimental

2.1. Synthesis of HGMBs loaded Fe-doped TiO_2 composite

All the chemicals used were analytically pure. The HGMBs were purchased from the Chem. Trading Co. Ltd., Guangdong. The nano-composites of Fe-doped TiO_2 (with Fe/Ti atomic ratio $x = 0$, 0.001, 0.005, 0.010 and 0.015, respectively) loaded on the HGMBs were prepared by the co-thermal hydrolysis deposition of titanium sulfate and iron nitrate in hot acidic water, followed by calcining treatment. In a typical experiment, firstly, 0.5 g HGMBs and 1 ml (0.1 M) sodium dodecyl sulphate organic ligand were added into a 100 ml beaker containing 20 ml H_2O as the stabilizing agent. The pH of the solution was then modulated to 2.0–3.0 by H_2SO_4. Secondly, 6 mmol $Ti(SO_4)_2$ and appropriate amount of $Fe(NO_3)_3$ were dissolved in 20 ml H_2O, then added into the above beaker in drops at the temperature of 100 °C. After the reaction, the composite product was filtrated, washed with deionized water and dried at 120 °C for 2 h, then calcined at 500 °C for another 2 h.

2.2. Characterization of the composite

The structures of the composite samples were measured by powder X-ray diffraction (XRD) on a Rigaku D/MAX2500 diffractometer with copper $K\alpha$ ($\lambda = 0.154$ nm) radiation. The composition, morphology and its evolution of TiO_2 were investigated by field emission scanning electron microscopy (FESEM, JSM-6700F), energy dispersive X-ray spectroscopy (EDS) and transmission electron microscopy (TEM, JEM-2010). The UV–Vis diffuse reflectance spectra were detected on a spectrometer (Lambda 900). The surface area measurements were carried out on a surface area and porosity analyzer (ASAP2020C+M), using the Barrett–Emmett–Teller (BET) technique.

2.3. Photocatalytic reaction

To characterize the photocatalytic activity of the nano-composites under visible light irradiation, experiments on photodegradation of methyl orange, a common contaminant in wastewater, were carried out at room temperature. Nano-composite of 100 mg, containing about 50% Fe-doped TiO_2 nanoparticles in weight, was put into a beaker containing 50 ml 10^{-5} M methyl orange water solution. A 300 W halogen lamp with a cut-off filter to remove the radiation below 420 nm was used as visible light source. The solution was magnetically stirred for 5 h in dark to establish the absorption/desorption equilibrium of methyl orange on the surfaces of the catalyst, then the light was turned on to initiate the photocatalysis reaction. After a certain period, 4 ml of the suspension was extracted and centrifuged at the rate of 6000 rpm for 5 min to remove the catalyst. The concentrations of the methyl orange before and after the photocatalytic degradation were measured with a UV–Vis spectrometer (Lambda 35).

3. Results and discussion

3.1. Microstructure of the composite

The XRD patterns of the bare HGMBs and the 500 °C calcined composite with $x = 0.010$ are shown in Fig. 1. For the bare HGMBs, the XRD pattern exhibits the typical amorphous feature with a diffuse hump at low diffraction angle. After calcining at 500 °C, the anatase TiO_2 (JCPDS No. 73-1764) emerges. Noticeably, no other crystalline phase is detected.

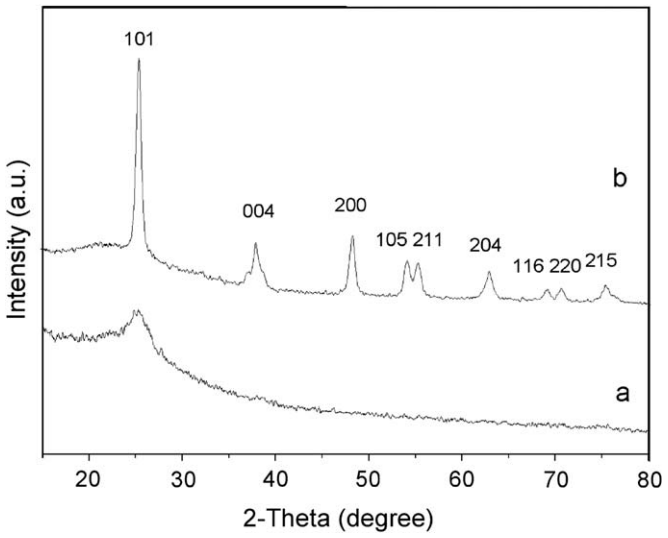

Fig. 1. XRD patterns of (a) the bare HGMBs and (b) the 500 °C calcined composite with $x = 0.010$.

The SEM images in Fig. 2 show the morphologies of the bare HGMBs and the 500 °C calcined composites with $x = 0.010$. The bare HGMBs exhibit integrated spheres with smooth surfaces, while a layer of rough material, which was identified as anatase TiO_2 by XRD measurement, was observed adhered to the HGMB for the 500 °C calcined composite. EDS spectrum taken from the TiO_2 layer on the surface of the HGMB, as presented in Fig. 2c, reveals the existence of Fe in TiO_2, with Fe: Ti molar ratio being about 1:100. In a comparative experiment of synthesizing TiO_2 without the addition of HGMBs, only the irregularly shaped TiO_2 microparticles were generated, as shown in Fig. 2d, verifying the role of HGMBs support in the formation of TiO_2 mesoporous layer.

In order to track the structure and morphology evolution of the composite during calcining treatment, more structural characterizations were performed on the samples with $x = 0.010$ calcined at various temperatures for 2 h, respectively. For the composite calcined at 200 °C, the surfaces of the HGMBs are adhered by a layer of agglomerate depositions (Fig. 3a), which is testified having basically the amorphous structure by the intense diffuse XRD hump presented in plot a of Fig. 4. When calcined at 300 °C, some particles precipitated from the amorphous matrix, as shown in the inset of Fig. 3b. They are anatase TiO_2 grains demonstrated by the crystalline peaks in plot b of Fig. 4. Further increase the temperature to 500 °C, more grains precipitated on the surfaces of the HGMBs, and the crystalline XRD peaks intensifies remarkably, indicating a better crystallization of anatase TiO_2. The cross sectional TEM image taken from a broken TiO_2 deposited HGMB, shown in Fig. 3d, reveals the porous feature of the deposited TiO_2 layer.

It is well known that both Ti^{4+} and Fe^{3+} ions can hydrolyze to form the amorphous hydroxide depositions in hot acidic water:

$$Ti(SO_4)_2 + 4H_2O \rightarrow Ti(OH)_4\downarrow + 2H_2(SO_4)_2 \quad (1)$$

$$Fe(NO_3)_3 + 3H_2O \rightarrow Fe(OH)_3\downarrow + 3HNO_3$$

The amorphous layer on the surfaces of the HGMBs consists of $Ti(OH)_4$ and small amount of $Fe(OH)_3$ depositions. The reason for the adherence of the amorphous depositions to the HGMBs might

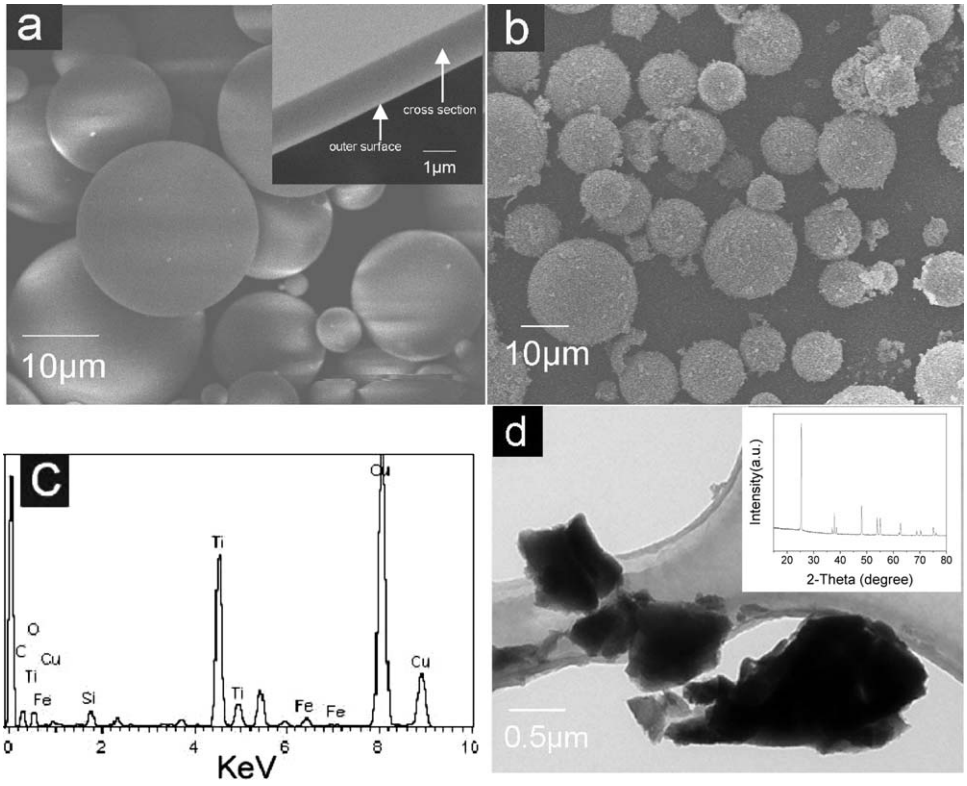

Fig. 2. (a) SEM image of the bare HGMBs, the inset shows the magnified micrograph of a piece of broken HGMB; (b) SEM image of the 500 °C calcined composite with $x = 0.010$; (c) EDS spectrum taken from the deposited layer of the 500 °C calcined composite; and (d) TEM image and XRD pattern of TiO_2 microparticles formed in a HGMBs-free reaction.

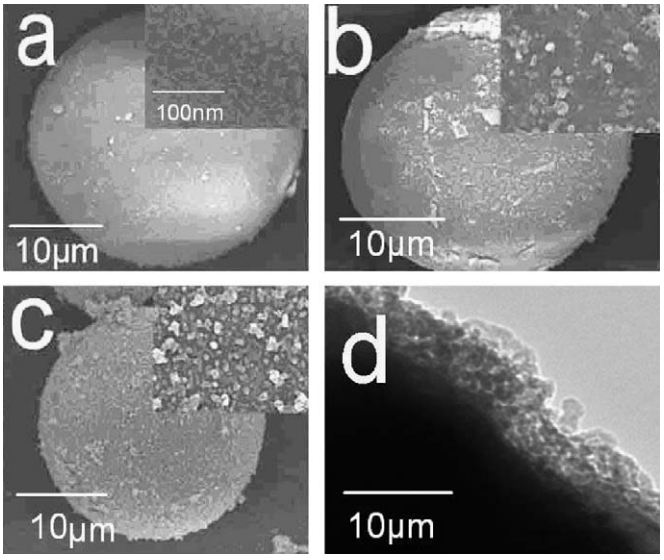

Fig. 3. (a)–(c) SEM images of the composites with $x = 0.010$, calcined at 200, 300 and 500 °C for 2 h, respectively; the insets show the magnified micrographs of the deposited layers at the same magnification. (d) cross sectional TEM image taken from a broken TiO_2 deposited HGMB.

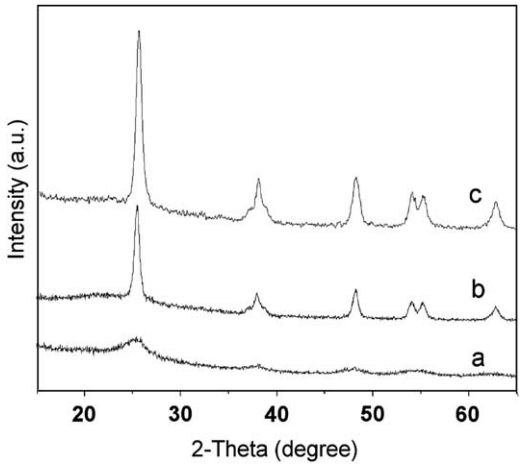

Fig. 4. XRD patterns of the composites with $x = 0.010$ calcined at (a) 200 °C; (b) 300 °C; and (c) 500 °C for 2 h respectively.

be the formation of the chemical bonds between Ti, Fe ions and O ions in the Si–O- and Al–O-groups at the surfaces of the HGMBs. When calcined at 300 °C or higher temperature, the amorphous hydroxides dehydrate and transform to the crystalline oxide, i.e., anatase TiO_2 doped with Fe which will be further illustrated later.

N_2 adsorption and desorption experiments of the composite with $x = 0.010$, calcined at 300 and 500 °C, respectively, were carried out to further characterize the porous structure of the crystallized TiO_2 layer on the surfaces of the HGMBs. The BET surface area was determined to be 30 m^2/g for the sample calcined at 300 °C, and 71 m^2/g for that calcined at 500 °C (as a comparison, the BET surface area for the bare HGMBs was 6 m^2/g). As demonstrated in Fig. 5, the N_2 adsorption and desorption isotherm is type IV with H_2 hysteresis-loop, characteristic of the mesoporous material for the 500 °C calcined sample [24]. The

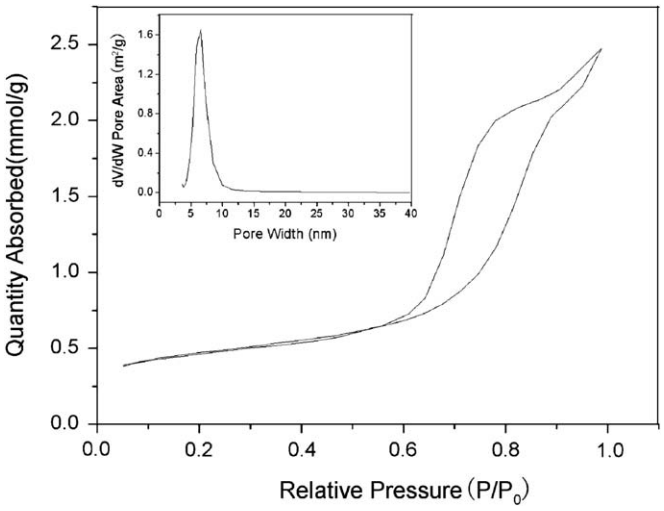

Fig. 5. N_2 adsorption and desorption isotherm of the 500 °C calcined composite with $x = 0.010$; the inset shows the pore-size distribution plot.

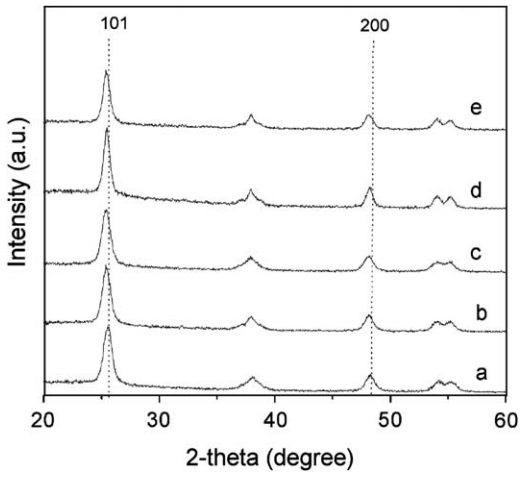

Fig. 6. XRD patterns of the 500 °C calcined samples with various Fe contents (x): (a) $x = 0$; (b) $x = 0.001$; (c) $x = 0.005$; (d) $x = 0.010$; and (e) $x = 0.015$.

inset in Fig. 5 reveals that the pore-size distribution (BJH) is narrow with mean pore width of 8 nm.

To testify the incorporation of Fe ions into the TiO_2 lattice, XRD measurements of the 500 °C calcined composites doped with various contents of Fe were performed, as shown in Fig. 6. Apparently, only one crystallization phase of anatase TiO_2 appears in all the samples. With gradual increase of Fe content in the composite, the positions of the TiO_2 peaks shift continuously towards the low-angle side. Taking the (101) peak as example, with x increasing from 0 to 0.015, the peak position shifts from 25.667° to 25.323°, indicating a slight lattice expansion. Using the XRD analysis software MDI Jade 5.0, the unit parameters (a, c) and the unit cell volume of the anatase TiO_2 in the composites with various content of Fe were calculated, which increase monotonously with Fe content, as presented in Table 1, implying the incorporation of Fe^{3+} ions into TiO_2 lattice probably by substituting Ti^{4+} ions. It is believed that, only a part of the added Fe ions in the reaction system are incorporated into the TiO_2 crystalline lattices, and the others are adsorbed on the surfaces of the TiO_2 nanocrystals, probably by forming Ti–O–Fe chemical bonds. The mean grain sizes in these samples evaluated by Debye-Scherrer formula are also listed in Table 1. They all have

Table 1
Unit cell parameters (a and b), unit cell volumes and grain sizes of anatase TiO_2 in 500 °C calcined samples doped with various content of Fe.

Fe content (x)	Unit cell parameters (Å)		Unit cell volume (Å^3)	TiO_2 grain size (nm)
	a	c		
0	3.7647	8.9608	127.00	12.0
0.001	3.7809	9.2227	131.84	13.4
0.005	3.7827	9.2992	133.06	12.6
0.010	3.7858	9.3447	133.93	16.4
0.015	3.7876	9.3448	134.06	12.3

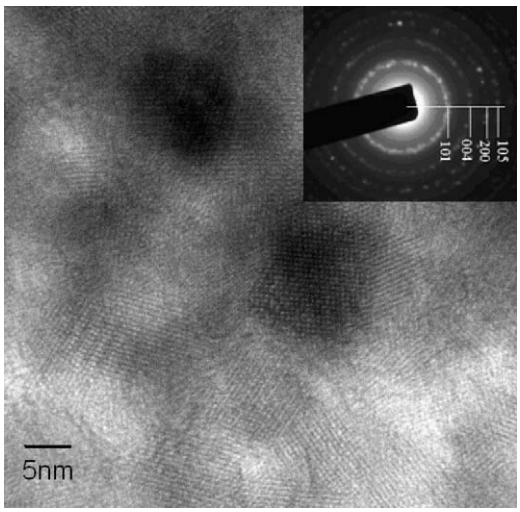

Fig. 7. HRTEM image and SAED pattern of TiO_2 nanoparticles taken from the cross section of a broken TiO_2 deposited HGMB with Fe content $x = 0.015$.

the value of 14.2 ± 2.2 nm, and seem to be not affected by Fe doping.

To exclude the possible iron rich phases in the composite, the high resolution TEM (HRTEM), selected area electron diffraction (SAED) and EDS analyses on the deposited layer were performed. HRTEM image exhibits clearly the crystallized nanoparticles, as shown in Fig. 7. EDS spectrum taken from this region is quite similar to the one presented in Fig. 2c, indicating the existence of Fe, while the corresponding SAED pattern, presented as inset in Fig. 7, reveals that besides anatase TiO_2 there is no other crystalline phase in this region. These results, together with those of XRD stated above, sufficiently exclude the generation of any iron rich crystalline phases in the composites.

3.2. Photocatalysis under visible light

The measured methyl orange photodegradation curves of the 500 °C calcined composites with various contents of Fe, under visible light irradiation, is presented in Fig. 8. C_0 and C are the concentrations of the methyl orange before and after irradiation. Obviously, the pure TiO_2 does not induce obvious change in methyl orange concentration, so the photosensitization of methyl orange is ignorable, while the Fe-doped TiO_2 exhibits the Fe-content dependent visible light photodegradation reaction. The photocatalytic rate increases with Fe content when $x \leq 0.010$, while it turns to decrease after $x > 0.010$. The catalyst with $x = 0.010$ yields the highest photocatalytic efficiency, with the degradation ratio of the 10^{-5} M methyl orange achieving 39% after

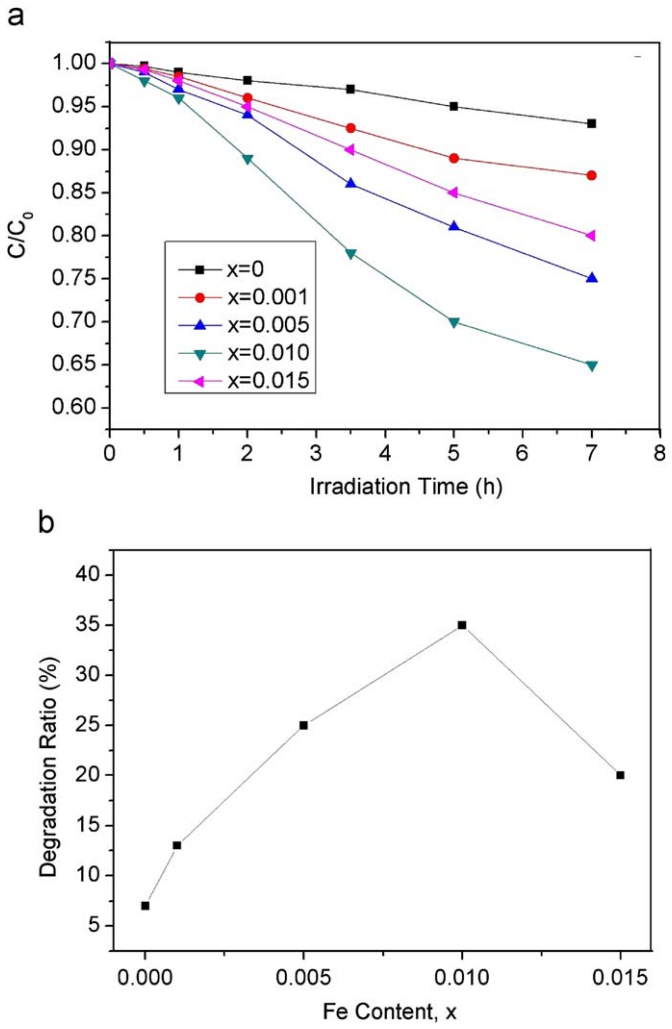

Fig. 8. (a) Photocatalytic degradation of methyl orange for the 500 °C calcined composite as a function of the visible light irradiation duration and (b) photocatalytic degradation ratio as a function of the doped Fe content.

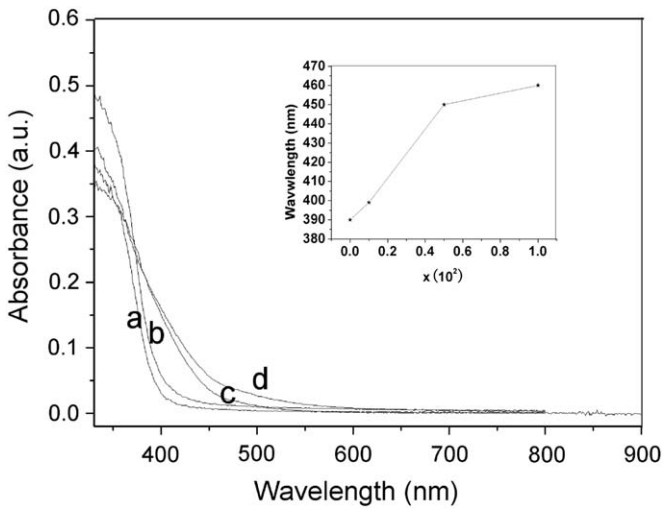

Fig. 9. UV–visible diffuse reflectance spectra of the 500 °C calcined composites doped with various content of Fe (x): (a) $x = 0$; (b) $x = 0.001$; (c) $x = 0.005$; and (d) $x = 0.010$; the inset shows position of the absorption edge as a function of Fe content.

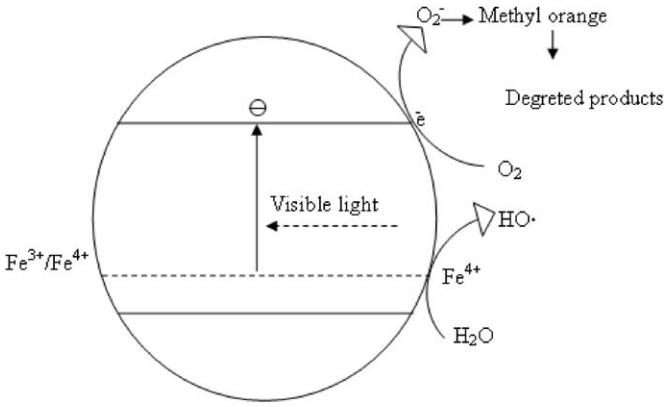

Fig. 10. Schematic diagram illustrating the mechanism of methyl orange degradation under visible light irradiation.

7 h irradiation under 300 W visible light. The visible light photocatalysis implies the red-shift of the TiO_2 absorption edge into the visible light region for the Fe doped composites, which is experimentally demonstrated by the UV–Visible diffuse reflectance spectra of the 500 °C calcined samples shown in Fig. 9. With the increase of Fe content in the composite, the TiO_2 absorption edge red-shifts remarkably, i.e., from UV into visible region (at about 460 nm for the sample with $x = 0.010$). Because the energy level of Fe^{3+}/Fe^{4+} lies a little above the valence band edge of TiO_2, as shown schematically in Fig. 10, the dopant energy level is induced with the doping of Fe^{3+} into TiO_2.[20] Fe^{3+} as an electron donor, its 3d electrons can be excited by the visible light to transit to the conduction band of TiO_2. These photogenerated electrons and the holes in the Fe^{4+} ions transfer to the surface of the photocatalyst to interact with the surrounding O_2, H_2O, etc., resulting in the formation of the highly activated free radicals, such as O_2^-, HO, etc., that oxidize the methyl orange. With increase of Fe content, the absorption edge of TiO_2 red-shifts to longer wavelength, thus more carriers are generated under visible light irradiation, which naturally induces the increase of the photocatalytic efficiency. However, since Fe^{4+} ions may also act as the recombination centers for the photogenerated carriers [20], when the doped Fe in TiO_2 exceeds a certain concentration, the photocatalysis is turn to be weakened due to the decrease of the photogenerated carriers.

4. Conclusions

The Fe-doped anatase TiO_2 mesoporous layer deposited on the hollow glass microbeads was prepared by a simple and green co-thermal hydrolysis method. The absorption edge of the semiconductor TiO_2 red-shifted obviously to the visible region, therefore the composites exhibited the effective visible light photocatalysis, with the highest photodegradation ratio of the 10^{-5} M methyl orange aqueous solution achieved 39% after 7 h irradiation under 300 W visible light ($\lambda > 420$ nm).

Acknowledgments

This work was supported by NSFC (50672098), the projects of CAS (KJCX2-YW-M05) and FJIRSM (SZD07004, 2006K02, 2006KL002).

References

[1] M.R. Hoffmann, S.T. Martin, W. Choi, D.W. Bahnemann, Chem. Rev. 95 (1995) 69.
[2] D.F. Ollis, C.R. Acad, C. R. Acad. Sci. Paris Se′rie IIc Chim. Chem. 3 (2000) 405.

[3] K. Tsujimaru, Eco-Mater. Process. Des. VII 510 (2006) 5.
[4] D.F. Ollis, E. Pellizzetti, N. Serpone, Environ. Sci. Technol. 25 (1991) 1522.
[5] K.J. Green, R.J. Rudham, J. Chem. Soc. Faraday Trans. 89 (1993) 1867.
[6] D. Bamba, P. Atheba, D. Robert, E. Trokourey, B. Dongui, Environ. Chem. Lett. 6 (2008) 163.
[7] J. Wu, S. Hao, J. Lin, M. Huang, Y. Huang, Z. Lan, P. Li, Cryst. Growth Des. 8 (2008) 247.
[8] W.X. Dai, X. Chen, X.P. Zheng, Z.X. Ding, X.X. Wang, P. Liu, X.Z. Fu, ChemPhysChem 10 (2009) 411.
[9] A.L. Linsebigler, G.Q. Lu, J.T. Yates, J. Chem. Rev. 95 (1995) 735.
[10] M. Mrowetz, W. Balcerski, A.J. Colussi, M.R. Hoffmann, J. Phys. Chem. B 108 (2004) 17269.
[11] J.C. Yu, J.W Yu, H.Z. Jiang, L. Zhang, Chem. Mater. 14 (2002) 3808.
[12] E. Bae, W. Choi, Environ. Sci. Technol. 37 (2003) 147.
[13] J.C. Kim, J.k. Choi, Y.B. Lee, J.H. Hong, J.I. Lee, J.W. Yang, W.I. Lee, N.H. Hur, Chem. Commun. (2006) 5024.
[14] H.G. Kim, D.W. Hwang, J.S. Lee, J. Am. Chem. Soc. 126 (2004) 8912.
[15] U.M. Khan Shahed, M. Al-Shahry, I.B. William Jr., Science 297 (2002) 2243.
[16] W.Y. Su, Y.F. Zhang, Z.H. Li, L. Wu, X.X. Wang, J.Q. Li, X.Z. Fu, Langmuir 24 (2008) 3422.
[17] H. Yamashita, M. Harada, J. Misaka, M. Takeuchi, K. Ikeue, M. Anpo, J. Photochem. Photobiol. A 148 (2002) 257.
[18] H. Yamashita, M. Harada, J. Misaka, M. Takeuchi, B. Neppolian, M. Anpo, Catal. Today 84 (2003) 191.
[19] X.B. Chen, S.M. Samuel, Chem. Rev. 107 (2007) 2891.
[20] W Choi, A. Termin, M.R. Hoffmann, J. Phys. Chem. 98 (1994) 13669.
[21] K.E. O'Shea, E. Pernas, J. Saiers, Langumuir 15 (1999) 2071.
[22] R.L. Pozzo, M.A. Baltanás, A.E. Cassano, Catal. Today 39 (1997) 219.
[23] Y. Kuwahara, T. Kamegawa, K. Mori, H. Yamashita, Chem. Commun. (2008) 4783.
[24] K.S.W. Sing, D.H. Evertt, R.A.W. Haul, L. Moscou, R.A. Pierotti, J. Rouquerol, T. Siemieniewska, Pure Appl. Chem. 57 (1985) 603.